JOURNAL OF AIRCRAFT
Vol. 38, No. 2, March–April 2001

Euler Solutions for Airfoils in Inhomogeneous Atmospheric Flows

Caroline Weishäupl* and Boris Laschka†
Technische Universität München, 85747 Garching, Germany

Inhomogeneous flows occuring naturally in the atmosphere and their influence on the flowfield around wing profiles are examined. Inhomogeneous, in this context, means that at least one flow variable has a spatial gradient, and, in particular, a gradient in the velocity component normal to the velocity vector is considered. Well-known examples for such flows are shear winds, jet streams, low-level jet streams, the flow situation near the ground, and microbursts. Numerical simulations are performed for a NACA 0012 airfoil using a finite volume Euler code. They focus on two cases, namely, an idealized shear wind for parameter studies and a microburst. For the idealized shear wind, a linear velocity change is assumed. In the subsonic case, the additional velocities on the lower and upper side of the airfoil result in a positive additional lift and a negative pitching moment around the 25% axis. In the transonic regime, the effect on shock strength and shock position is dominant. For simulation of the flight through a microburst, a potential model for the velocity field, consisting of a vortex ring parallel to the ground and a vortex ring of same strength mirrored at the ground, is applied. The chosen parameters simulate the Dallas–Fort Worth microburst. The analysis shows that the characteristics of the lift and moment coefficient follow that of the vertical velocity component, induced by the microburst. Rapid changes in the pitching moment with severe consequences on longitudinal stability occur.

Nomenclature

$\bar{\boldsymbol{A}}$ = Jacobian matrix for primitive variables (ξ direction)
a = altitude
c = speed of sound, coefficient
c_l, c_m = lift coefficient, pitching moment coefficient
c_p = pressure coefficient
e = total energy density, $p/(\kappa - 1) + \rho(u^2 + v^2)/2$
$\boldsymbol{F}, \boldsymbol{G}$ = fluxes in curvilinear coordinates ξ and η
J = determinant of the Jacobian of grid transformation
l = length, airfoil chord
M = Mach number
M_F = flight Mach number
M_l, M_u = lower and upper Mach number in the idealized shear wind
M_y = vertical component of Mach number
$\boldsymbol{n}$ = normal vector
$\boldsymbol{P}_k, \boldsymbol{P}_k^{-1}$ = matrix of the right and left eigenvectors of the nonconservative Euler equations
p = pressure
$\boldsymbol{Q}$ = vector of conservative variables times J
$\bar{\boldsymbol{Q}}$ = vector of primitive variables times J
q = dynamic pressure
t = time
$\boldsymbol{t}$ = tangential vector
u, v = velocity components in Cartesian coordinates x and y
$\boldsymbol{v}$ = velocity vector
$\boldsymbol{W}$ = vector of the characteristic variables
x_m = moment reference point
x_P, y_P = position of the airfoil
x_0, x_1 = start and end position for the flight through the microburst
y_0, y_1 = lower and upper boundary of the idealized shear wind
α = angle of attack
Δc_p = difference in pressure coefficient, $c_{p_{\text{inhom}}} - c_{p_{\text{hom}}}$
ΔM = change in incoming Mach number in the idealized shear wind
$\Delta M/\Delta y$ = vertical gradient of Mach number in the idealized shear wind
κ = ratio of specific heats
Λ = diagonal matrix of the eigenvalues of $\bar{\boldsymbol{A}}$
ξ, η = curvilinear coordinates
ρ = density
τ = transformed time due to coordinates ξ and η
τ_c = characteristic time
Ψ = stream function

Introduction

DURING flight, aircraft may be affected by inhomogeneous flows produced naturally in the atmosphere. These flows are difficult to foresee and are, therefore, of great importance concerning flight safety. Because of the hazard of windshears for flight safety, the International Civil Aviation Organization has introduced categories depending on the shear wind velocity gradient $\partial u/\partial y$ (Refs. 1 and 2). Gradients in the range of 0.066–0.13 s^{-1} are significant; in the range 0.13–0.2 s^{-1}, difficult; and above 0.2 s^{-1}, dangerous.

Phenomena of interest in this context are, for example, shear winds, jet streams, low-level jet streams, boundary layers, and microbursts. Jet streams are regions with strong wind occuring in the upper troposphere and stratosphere.[3] In comparison to jet streams, the gradients occurring in so-called low-level jet streams are considerably higher and reach values up to 0.15 s^{-1}. This phenomenon occurs in altitudes lower than 1.5 km (Ref. 4). Near the ground, inhomogeneous conditions occur as well. A turbulent boundary layer develops between the gradient wind and the surface, where the velocity decreases to zero.[5] Microbursts often come up in thunderstorms.[6] The associated flowfield pattern is characterized by a strong downwind, which impacts the ground and bursts out, causing strong horizontal winds.[7] During the flight through a microburst, the pilot faces a rapid change from headwind to tailwind combined with a strong downdraft. Many severe accidents in the past are connected with microbursts. Two of the most fatal ones are the crash of an L-1011

Presented as Paper 99-3587 at the AIAA 30th Fluid Dynamics Conference, Norfolk, VA, 28 June–1st July 1999; received 1 May 2000; revision received 22 September 2000; accepted for publication 30 September 2000.

*Chief Scientist, Lehrstuhl für Fluidmechanik. Member AIAA.

†The Chair, Institute of Fluid Mechanics, Lehrstuhl für Fluidmechanik. Honorary Fellow AIAA.

during landing in Dallas in August 1985[8–10] and that of a Boeing 727 in New York in June 1975.[6,9]

The awareness that windshears can become dangerous was reflected in different research activities in this field. Numerous weather studies like the 1982 Joint Airport Weather Studies were conducted to obtain extensive wind data in microbursts.[11,12] Windshear warning systems were developed.[13] Another important point for meteorology and aviation is the modeling of windshears, especially of microbursts. Concerning flight problems, relatively simple models, describing the velocity distribution in the microburst, are desirable. For the irrotational flow in the microburst, models based on the potential theory such as those using vortex rings are suitable. Such models were developed by several authors.[9,14–17] The parameters of the models have to be adapted to the measured data in real microbursts. In the field of flight mechanics, problems like the optimal flight path,[18,19] possible escape strategies,[8] and aircraft performance[20] are treated. Concerning the interference between the flowfield and the aircraft, apart from some fundamental studies, for example, those of Ruden,[21] Tsien,[22] and Weissinger,[23] only a few investigations, mainly based on experimental work,[24,25] exist up to now. An overview is given by Küchemann.[26]

Because of the aforementioned lack of investigations for inhomogeneous flows, this paper deals with two types of inhomogeneous flows, namely, a shear wind and a microburst. Shear winds characterized by a velocity gradient normal to the flow vector are rotational flows and cannot be simulated appropriately with potential methods. The steady flowfield of a microburst can be modeled as irrotational, but during the airfoil motion through the microburst unsteady conditions occur. In this case, straightforward potential methods are not widely available. Furthermore, for the simulations it is assumed that viscous effects associated with the velocity gradients of the incoming flowfield do not significantly change the aircraft pressure distributions and aerodynamic coefficients. Therefore, the Euler equations, describing inviscid rotational compressible unsteady flows, are the governing equations. The calculations are performed for a NACA 0012 airfoil using a finite volume Euler code with total variation diminishing (TVD) feature. Elliptic grid generation is used. After the validation, steady and unsteady results are given for an idealized shear wind with a linear velocity change, and extensive parameter studies are conducted. Subsequently, the unsteady flow conditions during the horizontal flight through a microburst are simulated.

Numerical Method

Solution of the Euler Equations

For two-dimensional flow, the conservative form of the unsteady Euler equations can be written in curvilinear coordinates ξ and η with unsteady metric terms (see Refs. 27 and 28),

$$\frac{\partial \boldsymbol{Q}}{\partial \tau} + \frac{\partial \boldsymbol{F}}{\partial \xi} + \frac{\partial \boldsymbol{G}}{\partial \eta} = 0 \tag{1}$$

with the vector of the conservative flow variables $\boldsymbol{Q}$ and the flux vectors $\boldsymbol{F}$ and $\boldsymbol{G}$

$$\boldsymbol{Q} = J\begin{pmatrix} \rho \\ \rho u \\ \rho v \\ e \end{pmatrix}, \qquad \boldsymbol{F} = J\begin{pmatrix} \rho U \\ \rho u U + \xi_x p \\ \rho v U + \xi_y p \\ U(e+p) - \xi_t p \end{pmatrix}$$

$$\boldsymbol{G} = J\begin{pmatrix} \rho V \\ \rho u V + \eta_x p \\ \rho v V + \eta_y p \\ V(e+p) - \eta_t p \end{pmatrix} \tag{2}$$

U and V denominate the contravariant velocities

$$U = \xi_x u + \xi_y v + \xi_t = \Theta_\xi, \qquad V = \eta_x u + \eta_y v + \eta_t = \Theta_\eta \tag{3}$$

and J the determinant of the Jacobian of the coordinate transformation[29]

$$J = \det(\boldsymbol{J}) = \det\left[\frac{\partial(x, y, t)}{\partial(\xi, \eta, \tau)}\right] = x_\xi y_\eta - x_\eta y_\xi \tag{4}$$

The metric terms can be written as[29,30]

$$\begin{aligned} &\xi_x = J^{-1} y_\eta, && \xi_y = -J^{-1} x_\eta, && \xi_t = -x_\tau \xi_x - y_\tau \xi_y \\ &\eta_x = -J^{-1} y_\xi, && \eta_y = J^{-1} x_\xi, && \eta_t = -x_\tau \eta_x - y_\tau \eta_y \end{aligned} \tag{5}$$

For the numerical solution, a finite volume formulation is chosen. Explicit time discretization is applied. The maximum possible time step is given by the Courant–Friedrichs–Lewy criterion. Because of this numerical limitation, the physical resolution in time is high enough. For the solution, dimension splitting is applied under the assumption that the fluxes normal to the cell faces are nearly independent from the fluxes parallel to the cell faces.[27] For the numerical flux at the cell face the TVD formulation of Yee, Roe and Davis[31] is used. To guarantee second-order discretization in space and to reduce to first order in regions of discontinuities, a minmod limiter is introduced. Furthermore, an entropy function avoids nonphysical expansion shocks.[31,32]

Boundary Conditions

To determine the boundary values, one can conclude from the characteristic theory that a physical boundary condition is necessary if the characteristic points into the evaluation region, otherwise a numerical boundary condition must be formulated. The characteristic equations are used as basis for both, the boundary conditions at the body and at the far field. Dealing with inhomogeneous flows, one cannot assume a priori local one-dimensional flow at the far field. Therefore, the far-field boundary conditions are formulated using the multidimensional characteristic equations. For that purpose, it is suitable to start from the Euler equations in primitive variables $\bar{\boldsymbol{Q}} = J\,(\rho, u, v, p)^T$ (Refs. 33 and 34),

$$\frac{\partial \bar{\boldsymbol{Q}}}{\partial \tau} + \bar{\boldsymbol{A}}\frac{\partial \bar{\boldsymbol{Q}}}{\partial \xi} + \bar{\boldsymbol{B}}\frac{\partial \bar{\boldsymbol{Q}}}{\partial \eta} = 0 \tag{6}$$

with the Jacobian matrices $\bar{\boldsymbol{A}}$ and $\bar{\boldsymbol{B}}$. After diagonalizing, one obtains

$$\frac{\partial \bar{\boldsymbol{Q}}}{\partial \tau} + \boldsymbol{P}_\xi \Lambda_\xi \boldsymbol{P}_\xi^{-1}\frac{\partial \bar{\boldsymbol{Q}}}{\partial \xi} + \boldsymbol{P}_\eta \Lambda_\eta \boldsymbol{P}_\eta^{-1}\frac{\partial \bar{\boldsymbol{Q}}}{\partial \eta} = 0 \tag{7}$$

with $\boldsymbol{P}$ as matrix of the right eigenvectors, $\boldsymbol{P}^{-1}$ that of the left eigenvectors, and Λ as diagonal matrix of the eigenvalues. Given the boundary $\xi = \text{const}$, the Euler equations are multiplied with $\boldsymbol{P}_\xi^{-1}$. If $\boldsymbol{P}_\xi^{-1}$ and $\boldsymbol{P}_\eta^{-1}$ are assumed constant, the following equation can be written for the boundary $\xi = \text{const}$:

$$\frac{\partial\left(\boldsymbol{P}_\xi^{-1}\bar{\boldsymbol{Q}}\right)}{\partial \tau} + \Lambda_\xi \frac{\partial\left(\boldsymbol{P}_\xi^{-1}\bar{\boldsymbol{Q}}\right)}{\partial \xi} + \boldsymbol{P}_\xi^{-1}\boldsymbol{P}_\eta \Lambda_\eta \boldsymbol{P}_\eta^{-1}\frac{\partial \bar{\boldsymbol{Q}}}{\partial \eta} = 0 \tag{8}$$

Analogously, for the boundary $\eta = \text{const}$, it follows that

$$\frac{\partial\left(\boldsymbol{P}_\eta^{-1}\bar{\boldsymbol{Q}}\right)}{\partial \tau} + \Lambda_\eta \frac{\partial\left(\boldsymbol{P}_\eta^{-1}\bar{\boldsymbol{Q}}\right)}{\partial \eta} + \boldsymbol{P}_\eta^{-1}\boldsymbol{P}_\xi \Lambda_\xi \boldsymbol{P}_\xi^{-1}\frac{\partial \bar{\boldsymbol{Q}}}{\partial \xi} = 0 \tag{9}$$

For the regarded boundary, the normal vector $\boldsymbol{n} = (\tilde{n}_x, \tilde{n}_y)^T$ pointing into the evaluation regime and the tangential vector $\boldsymbol{t}$ in counterclockwise direction are introduced. Then, the characteristic variables, which result from the product $\boldsymbol{P}_k^{-1}\bar{\boldsymbol{Q}}$, can be written as

$$J\boldsymbol{W} = J\begin{pmatrix} w_1 \\ w_2 \\ w_3 \\ w_4 \end{pmatrix} = J\begin{pmatrix} \rho - p/c^2 \\ \tilde{n}_y u - \tilde{n}_x v \\ \left(1/\sqrt{2}\right)[\boldsymbol{n}\cdot\boldsymbol{v} + p/(\rho c)] \\ \left(1/\sqrt{2}\right)[-\boldsymbol{n}\cdot\boldsymbol{v} + p/(\rho c)] \end{pmatrix} \tag{10}$$

With this notation, the characteristic equations in two-dimensional form can be derived from Eqs. (8) and (9), respectively,[33]

$$
\begin{aligned}
\left(\frac{\partial}{\partial \tau} + \boldsymbol{v}_r \cdot \nabla\right) w_1 &= 0 \\
\left(\frac{\partial}{\partial \tau} + \boldsymbol{v}_r \cdot \nabla\right) w_2 &= \frac{c}{\sqrt{2}}(\tilde{n}_x \partial_y - \tilde{n}_y \partial_x)(w_3 + w_4) \\
&= -\frac{1}{\rho}(\boldsymbol{t} \cdot \nabla) p \\
\left(\frac{\partial}{\partial \tau} + (\boldsymbol{v}_r + c\boldsymbol{n}) \cdot \nabla\right) w_3 &= \frac{c}{\sqrt{2}}(\tilde{n}_x \partial_y - \tilde{n}_y \partial_x) w_2 \\
&= -\frac{c}{\sqrt{2}} \boldsymbol{t} \cdot [(\boldsymbol{t} \cdot \nabla)\boldsymbol{v}] \\
\left(\frac{\partial}{\partial \tau} + (\boldsymbol{v}_r - c\boldsymbol{n}) \cdot \nabla\right) w_4 &= \frac{c}{\sqrt{2}}(\tilde{n}_x \partial_y - \tilde{n}_y \partial_x) w_2 \\
&= -\frac{c}{\sqrt{2}} \boldsymbol{t} \cdot [(\boldsymbol{t} \cdot \nabla)\boldsymbol{v}] \qquad (11)
\end{aligned}
$$

with $\boldsymbol{v}_r = (u - x_\tau, v - y_\tau)^T$ and $\nabla = (\partial/\partial x, \partial/\partial y)^T$. These equations are the basis for the applied boundary conditions, taking into account the gradient of the flow variables along the boundary. For the determination of the boundary values, we distinguish between inflow and outflow conditions. For subsonic two-dimensional flow, for the inflow case, three characteristics point into the flowfield and one outward. Analogously, for the outflow case, three characteristics point outward and one inward. Depending on the direction of the respective characteristic Eqs. (11) are discretized. If the characteristic points inward, the freestream values are used, if the characteristic points outward, the values of the first cell inside the field are used. From an adequate combination of the discretized equations, the boundary values for pressure, density, and the velocity components result. These are given completely in Ref. 32.

At the body, the kinematic boundary condition $\boldsymbol{v}_{\text{fluid}}\, \boldsymbol{n} = \boldsymbol{v}_{\text{contour}} \boldsymbol{n}$ has to be satisfied. This is the physical boundary condition for the characteristic pointing into the evaluation region. For the other three characteristics, numerical boundary conditions are applied. The values of the according characteristic variables are set equal to the values in the first cell inside the evaluation region.[32]

Validation

Experimental and numerical data for incompressible flow by Ludwig and Erickson[24] is taken for validation of the code applied to inhomogeneous flows. The investigations are performed for a symmetrical Joukowsky airfoil with 17% relative thickness. The theory is based on the solution of the equation for the stream function in two-dimensional incompressible inviscid shear flow $\nabla^2\Psi = f(\Psi)$ (Ref. 24). In addition to the theoretical studies, results of corresponding wind-tunnel tests are available.

A piecewise linear velocity profile acting on the Joukowsky airfoil positioned in a channel is considered (Fig. 1). The given lengths are expressed with respect to the airfoil chord l. The grid used consists of 5800 cells with 60 cells for each airfoil side and a distance of the first off-body grid points of $0.001l$. For the numerical simulation with an Euler code for compressible flow, the freestream conditions ($M_m = 0.1075$, $M_{\min} = 0.0967$, and $M_{\max} = 0.1182$) of Ref. 24 are transformed to a higher Mach number because otherwise convergence problems occur in the simulation. The transformation ensures that the flow remains approximately incompressible and that the shear wind is conserved in level and gradient. Therefore, the simulations are conducted for the parameters $M_m = 0.3$, $M_{\min} = 0.27$, $M_{\max} = 0.33$, $a = 0.5$, and $\alpha = 5.7$ deg (see Fig. 1). The altitude a is given for the airfoil midchord. Additionally, the results of the Euler simulations are transformed with the Prandtl–Glauert rule to the original case.

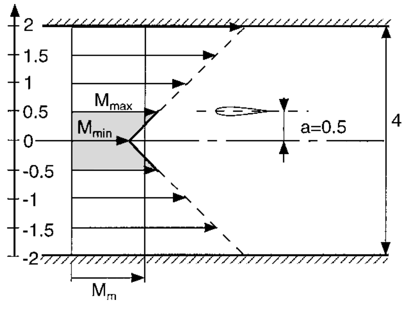

Fig. 1 Geometry and parameters of the validation case for a Joukowsky airfoil.[24]

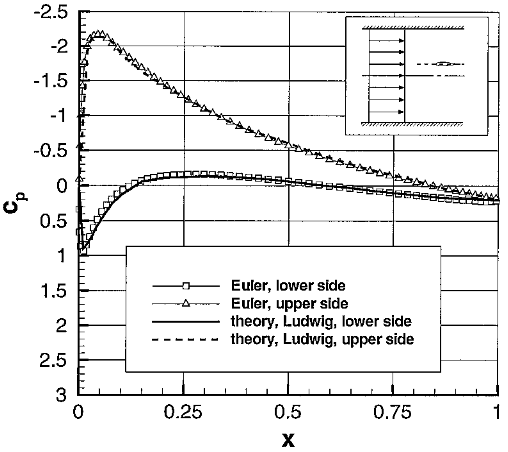

a) Homogeneous flow

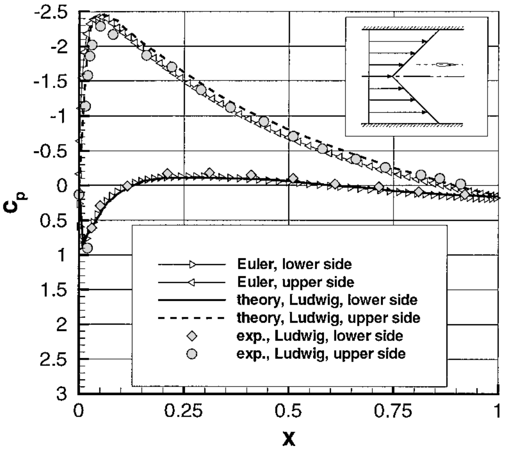

b) Inhomogeneous flow: Euler, c_l = 0.8720; Tsien,[22] c_l = 0.8018

Fig. 2 Pressure distribution c_p for the validation case Ref. 24 (Joukowsky, δ = 17% and α = 5.7 deg).

To begin with homogeneous flow, the pressure distributions of the Euler code and of the theory of Ref. 24 agree very well (Fig. 2a). Because of the velocity gradient, in the inhomogeneous case the pressure minimum increases on the upper side and decreases slightly on the lower side (Fig. 2b). The results of the Euler code and the theoretical and experimental results of Ref. 24 again show very good agreement. Possible reasons for the small deviations can be viscous effects in the experiment that cannot be reproduced by the Euler code or compressible flow effects resulting from the Euler code.

Furthermore, these numerical results can be compared with the exact solution for symmetrical Joukowsky airfoils in shear flow presented by Tsien.[22] Based on a suitable stream function with respect to a linear velocity profile, the lift and moment coefficient can be calculated as function of the airfoil thickness, the angle of attack, and the shear wind gradient. The method of Tsien and the simulations performed here differ mainly in the following two ways: First, instead of the linear velocity profile of Tsien, here piecewise linear velocity or Mach number profiles, respectively, are considered. Second, the exact solution of Tsien is valid for incompressible flow, but here compressible flow is the point of interest. In spite of these differences, the exact values given by Tsien can be given as a basic reference for the simulations. Considering the aforementioned velocity gradient, a lift coefficient of $c_l = 0.8018$ results for the 17% Joukowsky airfoil at $\alpha = 5.7$ deg. The value obtained from the Euler simulation is $c_l = 0.8720$. With regard to the mentioned differences between the two approaches, the agreement of the results is satisfying. Further validation cases are given in Ref. 32.

Results

The subsequent investigations focus on two important cases of inhomogeneous flows. First, an idealized shear wind with linear velocity change is analyzed in the subsonic and transonic velocity regime with the dominant parameters varied. Second, the horizontal flight through a microburst is simulated. All simulations are performed for a NACA 0012 airfoil. The steady simulations are assumed to be converged if the maximum occurring density change falls below the limit of 10^{-6}. More details and further results are given in Ref. 32.

For grid generation, an elliptic Poisson algorithm is applied.[35–38] With a multiblock topology, it is possible to realize a C topology near the wing and at the same time linear far field boundaries (Fig. 3a). The standard 12-block grid consists of 5300 cells with 60 cells on each airfoil side and a distance of the first off-body grid points of $0.005l$ (Fig. 3b). For the farfield distance, 20 chords are chosen. To consider the influence of the grid resolution, a fine grid with 120 cells on each airfoil side, a $0.0025l$ distance of the first off-body grid points and 21,200 cells are employed.

Idealized Shear Wind

To study the general influence of inhomogeneous incoming flow on an airfoil, the following idealized conditions are assumed: The airfoil is positioned in a steady shear wind field with the Mach number of incoming flow changing linearly from 0 to ΔM in the region $[y_0, y_1]$. For a sufficient resolution, the grid used is optimized, with the grid lines concentrated in the shear wind region. The airfoil moves horizontally with the flight Mach number M_F, and in the unsteady case an additional vertical velocity component M_y occurs (see Fig. 4a). For the numerical simulation, the flight Mach number and the shear wind can be superposed to the Mach number $M(y)$ dependent on the altitude y with

$$M(y) = \begin{cases} M_F = M_l & \text{where } y < y_0 \\ M_F + [(y - y_0)/(y_1 - y_0)]\Delta M & \text{where } y_0 \le y < y_1 \\ M_F + \Delta M = M_u & \text{where } y \ge y_1 \end{cases} \qquad (12)$$

M_l denominates the Mach number below the shear wind region and M_u the Mach number above this region (Fig. 4b). All values for y are expressed with respect to to the airfoil chord l.

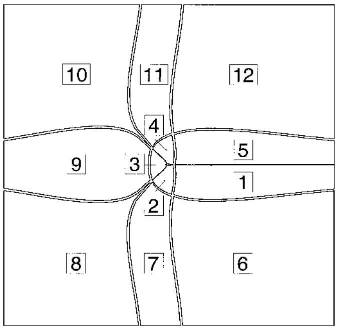

a) Block topology

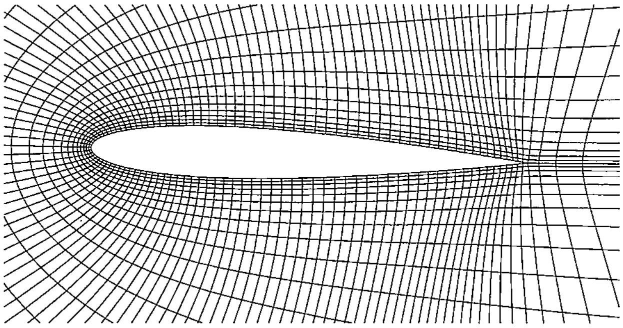

b) Detail near the airfoil

Fig. 3 NACA 0012 airfoil 12-block grid.

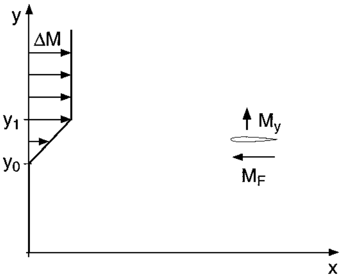

a) Incoming flowfield with linear velocity change

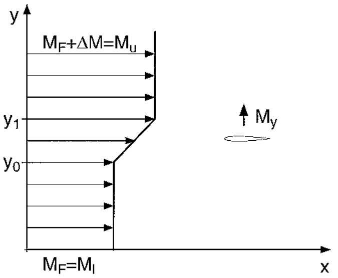

b) Interpretation for numerical simulation

Fig. 4 Flow situation in the idealized shear wind.

For describing the obtained results, it is necessary to choose a useful reference Mach number. All of the following results for the idealized shear wind are related to the constant horizontal flight Mach number $M_F = M_l$. This has to be considered for interpretation of the pressure, lift, and moment coefficient. Because of the constant reference Mach number M_F, local higher Mach numbers lead to a higher dynamic pressure and, consequently, to higher coefficient values than for reference to the respective local Mach number $M(y)$. To obtain the value of the coefficient c with respect to the varying incoming Mach number $M(y)$ from the value referred to M_F, the following formula can be applied

$$c[M(y)] = \left[q_{M_F} / q_{M(y)}\right]c = \left[M_F^2 / M^2(y)\right]c \qquad (13)$$

Both regions, the subsonic and transonic flow regimes, are investigated with the flight Mach numbers $M_F = 0.4$ and 0.7, respectively. For the change of Mach number in the shear wind, a high value of $\Delta M = 0.1$ is chosen to get significant effects. Realistic gradients occurring in the atmosphere are much smaller. The lower bound of the shear wind lies in all cases at $y_0 = 2$. The basis for the performed parameter variations is the following reference case: The shear wind covers a vertical distance of $\Delta y = y_1 - y_0 = 0.5$, which corresponds to a gradient of $\Delta M/\Delta y = 0.2$. The airfoil is positioned with zero angle of attack in half-altitude of the shear wind.

First, the flow situation due to the idealized shear wind is regarded in the steady case for the subsonic regime. The distribution of the pressure coefficient c_p for the reference case is compared to homogeneous incoming flow with the mean Mach number $M_\infty = (M_l + M_u)/2 = 0.45$ (Fig. 5). For consistency, the values belonging to the homogeneous case are also referred to $M_F = 0.4$. Because of the positive shear wind gradient, the pressure minimum is increased on the upper side and decreased on the lower side in comparison to the homogeneous flow. Therefore, a positive additional lift and a negative additional moment around $x_m = 0.25$ result. To estimate the influence of the grid resolution, the reference case is also simulated with a fine mesh consisting of 21,200 cells compared to 5300 cells of the standard grid used. The pressure distributions for the standard and the fine grid (Fig. 5) show only small

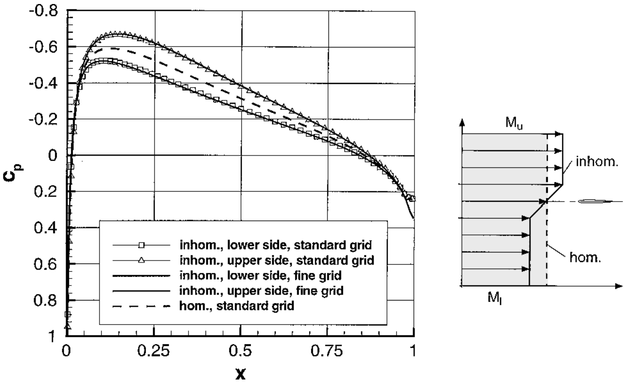

Fig. 5 Steady pressure distribution c_p for the NACA 0012 airfoil in subsonic inhomogeneous flow (M_F = 0.4, $\Delta M/\Delta y$ = 0.2, and α = 0 deg).

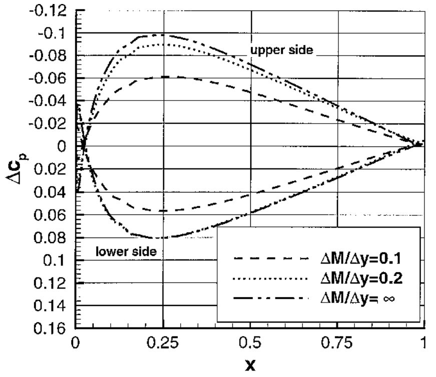

a) Difference in the pressure coefficient Δc_p between inhomogeneous and homogeneous (M_∞ = 0.45) flow

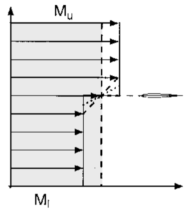

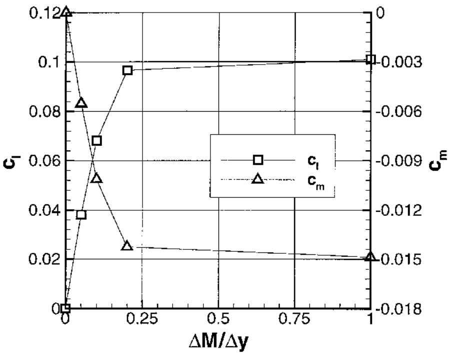

b) Lift and moment coefficients c_l and c_m

Fig. 6 Steady coefficients in subsonic inhomogeneous flow (M_l = 0.4, M_u = 0.5, and α = 0 deg) for different shear wind gradients $\Delta M/\Delta y$.

deviations in the region of the pressure minimum on the lower and the upper side and the recompression region at the trailing edge. The lift and moment coefficient for the fine grid are $c_l = 0.1012$ and $c_m = -0.01505$, in comparison to $c_l = 0.0965$ and $c_m = -0.01426$ for the standard grid.

The shear wind gradient and the position of the airfoil in the shear wind are important parameters. Concerning steady flow, the difference of the pressure distribution $\Delta c_p = c_{p_{\text{inhom}}} - c_{p_{\text{hom}}}$ between the inhomogeneous and homogeneous ($M_\infty = 0.45$) case is regarded for several gradients, namely, $\Delta M/\Delta y = 0.1, 0.2$, and ∞ (see Fig. 6a). With increasing gradient, the difference Δc_p grows, whereby on the upper side the deviation is bigger than on the lower side. Above a certain gradient value, only small changes occur in the flow around the airfoil, if the gradient is increased further. Therefore, the lift and moment coefficient remain then nearly constant up to the limit value belonging to the Mach number jump $\Delta M/\Delta y = \infty$ (see Fig. 6b).

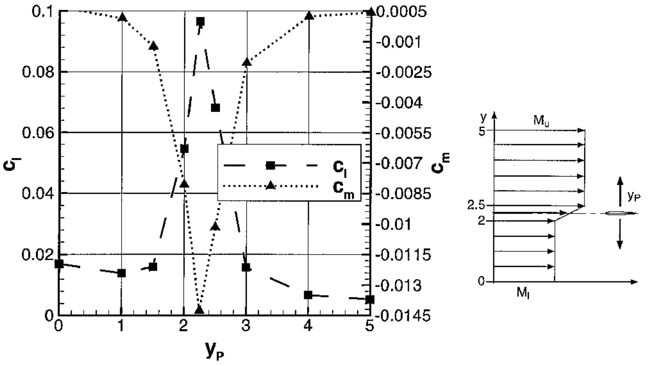

Fig. 7 Steady lift and moment coefficients c_l and c_m for subsonic inhomogeneous flow (M_l = 0.4, M_u = 0.5, α = 0 deg, and $\Delta M/\Delta y$ = 0.2) for different airfoil positions y_P.

With regard to the influence of the airfoil position y_P, a positive additional lift and a negative moment already appear in the vicinity of the shear wind region (Fig. 7). As they approach the center of the shear wind, these values increase up to the extreme value.

In the next step, an additional vertical motion of the airfoil with the vertical Mach number component M_y is regarded. For the simulation of the vertical motion the airfoil has to be moved through the inhomogeneous flowfield. The grid has to be adapted to the actual airfoil position at each time step. This adaptation can be performed in the following two ways: In the first adaptation, only the airfoil itself moves within the grid, whereby the far-field boundaries remain fixed in space. Consequently, the grid is deformed during the motion. This method is suitable for small distances or if only parts of the body move. The alternative is to move the whole grid with the airfoil vertical velocity through the flowfield. In this case the grid remains undeformed. For the simulation of the motion through inhomogeneous fields, long distances have to be covered. Therefore, in this case a motion of the whole grid through the inhomogeneous field is more suitable than the relative motion of the airfoil inside the grid to guarantee constant grid quality and to avoid large cell deformations. Depending on the instantaneous position, the values of the flow variables at the far-field boundaries are then evaluated from Eq. (12). From there, the information propagates into the computational domain. The regarded motions start from $y = 0$ and end at $y = 5$. As the initial field for the unsteady simulation, the steady-state result at $y_P = 0$ is used. Without a suitable start solution, oscillations occur in the unsteady lift and moment coefficient in the beginning. With regard once again to the reference case ($\Delta M/\Delta y = 0.2$ and $\alpha = 0$ deg), the unsteady behavior for two vertical Mach numbers $M_y = 0.01$ and 0.02 is compared with the quasisteady behavior. As mentioned earlier, the constant reference Mach number $M_F = M_l$ is used. The unsteady characteristics for the lift and moment coefficient (Fig. 8) can be subdivided into three parts: 1) the response to the Heaviside function in the vertical Mach number starting from the steady values for $y_P = 0$ (Fig. 7) and the motion through the homogeneous field with $M(y) = M_l$, 2) the passing through the shear field, and 3) the motion through the homogeneous part with $M(y) = M_u$. The following general effects can be detected: Because of the vertical motion upwards and the corresponding relative flow downwards, a negative lift coefficient occurs during the motion. Therefore, the values of c_l and c_m change immediately after the start of the unsteady simulation. In the shear wind region, the local negative angle of attack due to the vertical motion decreases because of the higher horizontal velocity $M(y)$. Therefore, additionally a positive lift and a negative moment come up in this region. At the same time, the increasing dynamic pressure leads to higher absolute values of the coefficients regarding the constant reference Mach number. Additionally, it has to be considered that the force component in the horizontal direction is given as the drag coefficient and that in the vertical direction as the lift coefficient, although the angle of attack varies during the motion. With an increase in the vertical Mach number M_y, the shear wind induced

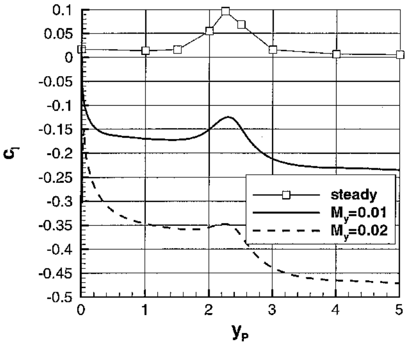

Lift coefficient c_l

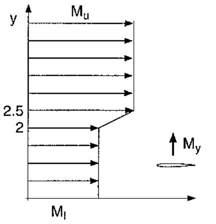

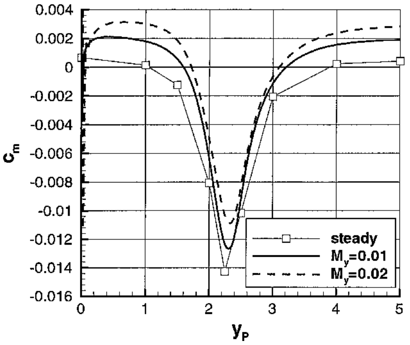

Moment coefficient c_m

Fig. 8 Unsteady characteristics of the lift and moment coefficient c_l and c_m for subsonic inhomogeneous flow (M_l = 0.4, M_u = 0.5, α = 0 deg, and $\Delta M/\Delta y$ = 0.2) during vertical motion with various vertical Mach numbers M_y.

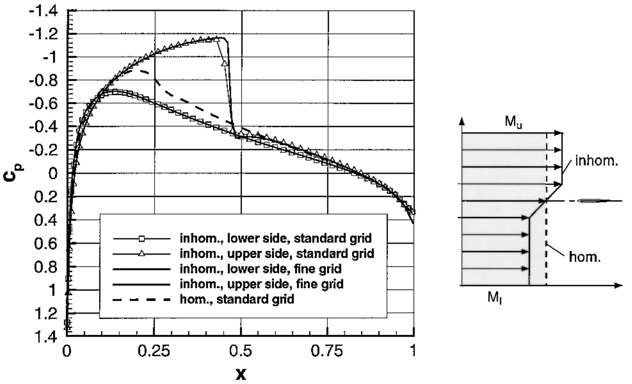

Fig. 9 Steady pressure distribution c_p for the NACA 0012 airfoil in transonic inhomogeneous flow (M_F = 0.7, $\Delta M/\Delta y$ = 0.2, and α = 0 deg).

maximum in lift is weakened. This is caused by the dominance of the increasing relative angle of attack over the shear wind and the smaller available time to build up the extremum. Furthermore, it is remarkable that the unsteady behavior of the moment coefficient is approximated well by the quasi-steady one.

In the transonic region, the idealized shear wind is investigated for the flight Mach number $M_F = 0.7$. With regard once again to the reference case ($\Delta M/\Delta y = 0.2$ and $\alpha = 0$ deg) in comparison to homogeneous incoming flow with $M_\infty = (M_l + M_u)/2 = 0.75$, the pressure distributions given in Fig. 9 result, referred to $M_F = 0.7$. For homogeneous flow, a weak shock occurs at about 25% of the airfoil chord. In inhomogeneous flow, the stagnation point is shifted downwards on the lower side. The velocity on the lower side is reduced, and the shock vanishes. On the upper side, the velocity and, with that, the pressure minimum increase. A shock results at about 45% of the airfoil chord. As in the subsonic case, an additional positive lift and a negative pitching moment develop, but their values change much more than in the subsonic case. Regarding the solution on the fine grid with 21,200 cells only small deviations from the solution for the standard grid can be detected. The corresponding coefficients are $c_l = 0.1737$ and $c_m = -0.02175$ for the standard grid and $c_l = 0.1755$ and $c_m = -0.02211$ for the fine grid.

As in the subsonic regime, the shear wind gradient is one important parameter. The difference of the pressure distribution Δc_p between the inhomogeneous and the homogeneous ($M_\infty = 0.75$) case is significantly influenced by the gradient, as depicted in Fig. 10 for $\Delta M/\Delta y = 0.1, 0.2$, and ∞. Higher gradients lead to higher deviations Δc_p from the homogeneous flow. On the upper side, the shock strength increases, and the shock moves downstream. Analogously, the pressure minimum on the lower side is reduced. Again, the influence on the upper side is higher than on the lower side as already detected in the subsonic flow region. The differences between $\Delta M/\Delta y = 0.2$ and ∞ are small. For increasing gradients, the values for the Mach number jump are asymptotically reached. Because of the influence of the shocks, the occurring changes are higher than in the subsonic case. Varying the position of the airfoil in the shear wind, the same tendencies as in the subsonic regime can be observed, but again the changes are of higher magnitude.

With respect to the angle of attack as a further important parameter, the difference Δc_p between inhomogeneous ($\Delta M/\Delta y = 0.2$) and corresponding homogeneous flow is analyzed for $\alpha = 0$, 1, and 2 deg (Fig. 11). With an increase in angle of attack, Δc_p is increased on the upper side and decreased on the lower side. In comparison to the homogeneous flow, a slightly stronger shock and the shock displacement downstream on the upper side are significant.

Microburst

Initially, the microburst was defined by Fujita[39] as a downwind that impacts on the ground and bursts out to hazardous horizontal winds with a horizontal extension lower than 4 km. The lifetime

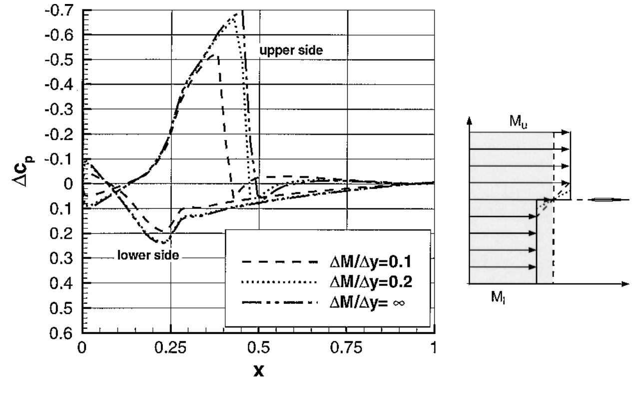

Fig. 10 Difference in the pressure coefficient Δc_p between inhomogeneous (M_l = 0.7, M_u = 0.8) and homogeneous (M_∞ = 0.75) steady flow with α = 0 deg for different shear wind gradients $\Delta M/\Delta y$.

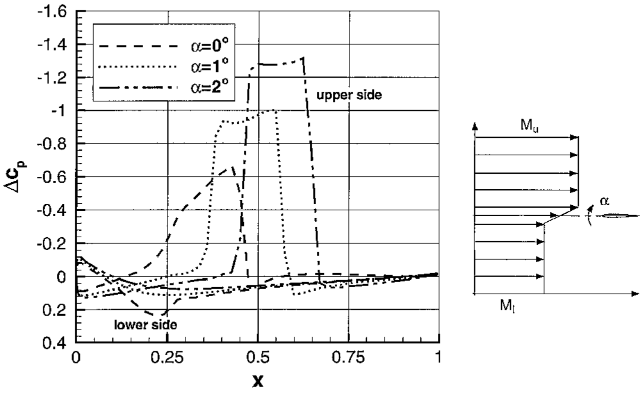

Fig. 11 Difference in the pressure coefficient Δc_p between inhomogeneous (M_l = 0.7, M_u = 0.8) and homogeneous (M_∞ = 0.75) steady flow with $\Delta M/\Delta y$ = 0.2 for different angles of attack α.

of microbursts lies in the range of 2–5 min. The changing wind conditions during the flight through a microburst, namely, the strong downwind combined with the rapid change from head- to tailwind, are difficult for the pilot to manage. Adequate models describing the characteristic flowfields are needed for microburst prediction and identification and for flight performance and control during flights through microbursts. Models based on the potential theory using vortex rings such as the model of Schultz,[14] which is applied here, are suitable. In this model a vortex ring parallel to the ground surface is used. To simulate the ground itself, a mirrored vortex ring of same strength is introduced (see Fig. 12). The velocity field obtained from the potential model is corrected inside the vortex core with a damping factor to consider viscous effects.

The velocity components are derived from the stream function Ψ, depending on the radius R of the vortex ring, the diameter of the viscous core d, the circulation of the vortex ring Γ, and the altitude of the vortex ring above the ground z. The corresponding equations are given in Refs. 14 and 32. To simulate a realistic flowfield, the values of the parameters are chosen according to the data of the Dallas–Fort Worth microburst[14] causing the crash of an aircraft in Dallas 1985. With an airfoil chord of 5 m as reference length, the dimensionless parameters for the simulation here are fixed to $R = 100$, $d = 60$, $\Gamma = 4$, and $z = 140$. For the presented two-dimensional Euler calculations, the most critical case, namely, the flight in the plane that contains the central axis of the microburst, is regarded.

The numerical simulation of the flight through the microburst is realized as depicted in Fig. 13. The discretized evaluation regime around the NACA 0012 airfoil (the whole grid) is moved through the microburst field along the flight path with the flight Mach number M_F. The freestream velocity values at the far-field boundaries are determined from the potential model for the microburst, dependent on the actual boundary position. In this case, the unsteady simulation is started directly with the undisturbed values obtained from the microburst model. A larger discretized evaluation region is not necessary because the influence of the inhomogeneous flow on the airfoil decreases with increasing distance. The flight starts at $x_0 = 300$, ends at $x_1 = -300$, and takes place at a constant altitude of $a = 115$.

During the flight, the microburst-induced components of horizontal and vertical velocity in the altitude of the flight path are important (see Fig. 14). The horizontal velocity (Fig. 14a) first leads to a headwind, increasing to a maximum and afterwards going down to zero, and in the next phase to an analogous tailwind. With regard to the vertical velocity (Fig. 14b), a small upwind component in the beginning is followed by a strong downwind component and finally again by an upwind component. Therefore, during the flight, first

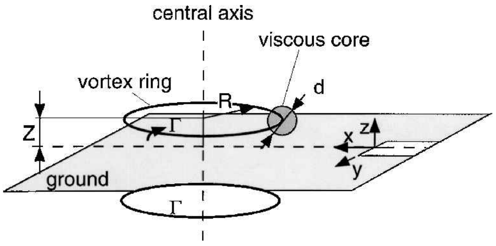

Fig. 12 Potential model for a microburst from Ref. 14.

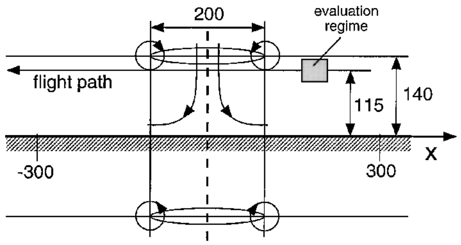

Fig. 13 Numerical simulation of the microburst.

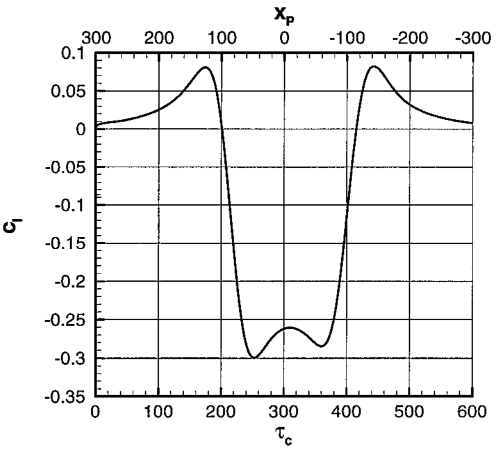

Lift coefficient c_l

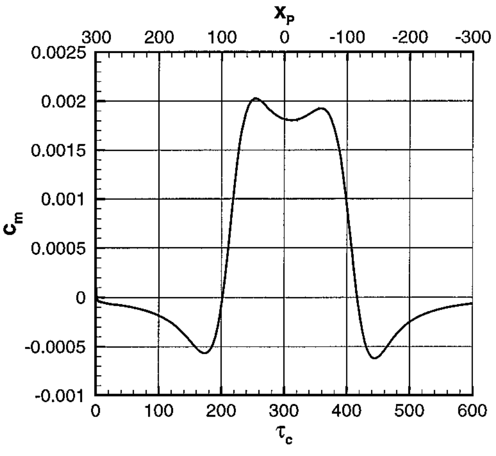

Moment coefficient c_m

Fig. 15 Unsteady characteristics of the lift and moment coefficients c_l and c_m for subsonic flight ($M_F = 0.4$) with $\alpha = 0$ deg through the simulated microburst.

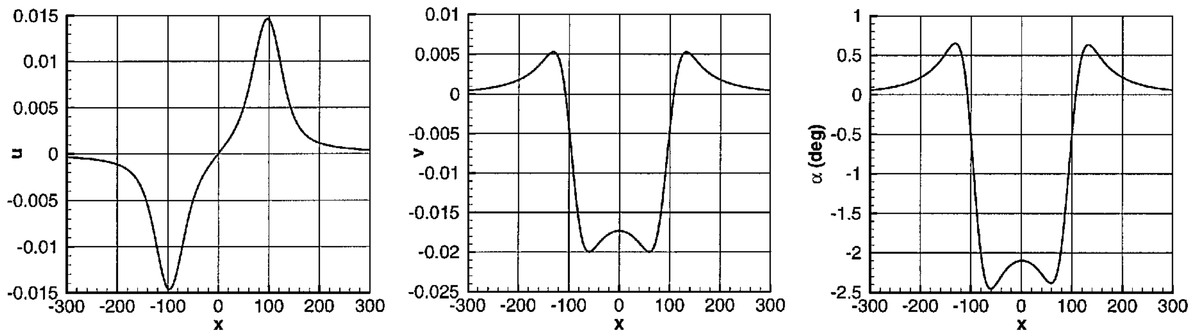

a) Horizontal velocity u

b) Vertical velocity v

c) Angle of attack α

Fig. 14 Microburst induced velocity components u and v and angle of attack α along the flight path ($a = 115$).

the angle of attack (Fig. 14c) increases, then strongly decreases, and in the end increases again. During the headwind, the whole horizontal velocity is increased, and, therefore, smaller absolute values for the angle of attack result than for tailwind. On the other hand, the higher horizontal velocity in the headwind region causes higher absolute values for the pressure and force coefficients due to the higher dynamic pressure.

The horizontal flight of a NACA 0012 airfoil at zero angle of attack and a subsonic Mach number of $M_F = 0.4$ is considered. For evaluation of the coefficients, the constant horizontal flight Mach number is chosen as reference value. The unsteady characteristics of the lift and moment coefficient (Fig. 15) reflect the behavior of the vertical wind and of the angle of attack, respectively, with a certain time delay. The position of the airfoil x_P corresponds to a characteristic time τ_c, which is also given in Fig. 15. The horizontal velocity component has only a small influence on the flowfield and aerodynamic forces because the maximum horizontal velocity induced by the microburst is only about 3% of the velocity belonging to the flight Mach number M_F. Against that, the maximum vertical component induces a significant change in angle of attack of nearly 2.5 deg. With respect to the extreme values of the lift and moment coefficient belonging to the extreme values of negative angle of attack, the values for the tailwind are smaller than for the headwind. This results from the higher dynamic pressure in the headwind region, which has more influence than the higher values of angle of attack for the tailwind. In the region with positive angles of attack, the difference between the values in head- and tailwind is small because the force coefficients are small too. The strong variations in lift are important for flight safety, especially with rapid changes between nosedown and taildown moments, which have to be considered carefully for flight control. To visualize the flowfield, the distribution of the vertical velocity and the streamlines coming up from the microburst are shown in Fig. 16 for two different characteristic times τ_c. Figure 16a shows a case in the beginning of the penetration with up- and headwind. In Fig. 16b, the strong downwind combined with a headwind can be detected.

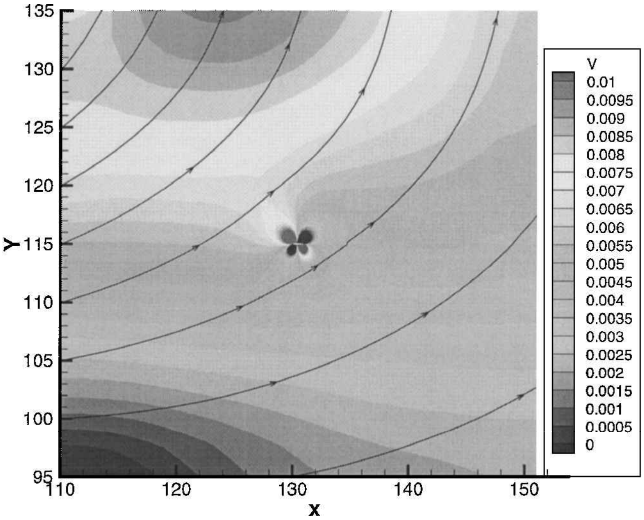

a) $x_P = 130$ ($\tau_c = 170$)

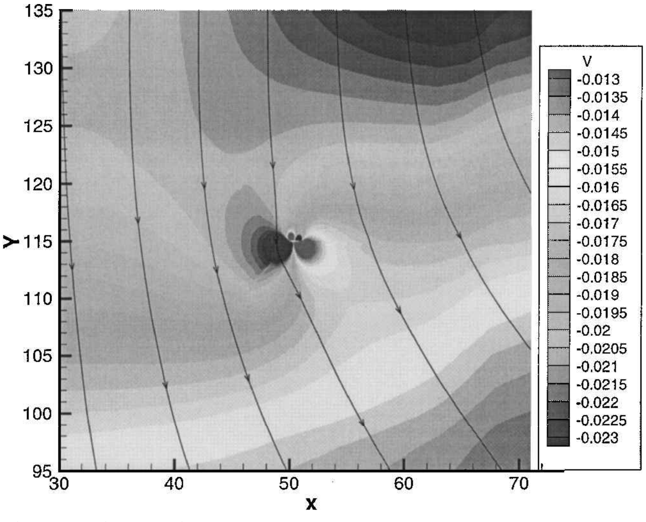

b) $x_P = 50$ ($\tau_c = 250$)

Fig. 16 Contour plots of the vertical velocity component v and streamlines for the subsonic flight (M_F = 0.4) with α = 0 deg through the simulated microburst.

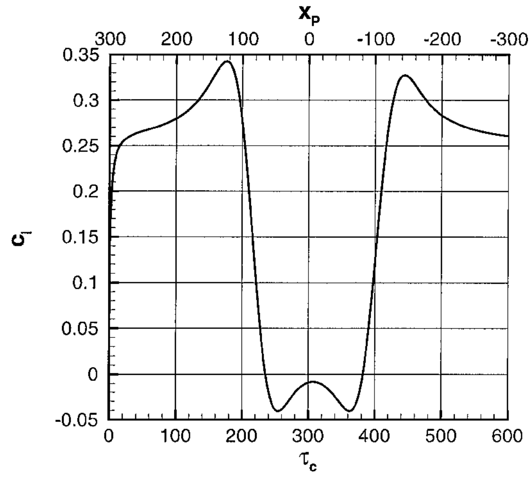

Lift coefficient c_l

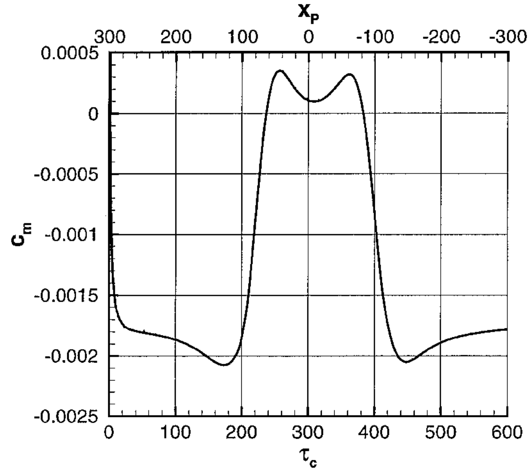

Moment coefficient c_m

Fig. 17 Unsteady characteristics of the lift and moment coefficient c_l and c_m for subsonic flight (M_F = 0.4) with α = 2 deg through the simulated microburst.

The characteristics of lift and moment coefficient for an angle of attack of 2 deg (Fig. 17) are similar to those for 0 deg, shifted for the lift coefficient to more positive values and for the moment coefficient to more negative values. Again, the coefficients are higher for the headwind than for the tailwind due to the higher dynamic pressure. Compared against $\alpha = 0$ deg, for $\alpha = 2$ deg, the difference in the values for the extreme positive angles of attack is higher than for the extreme negative ones due to the higher absolute values of the force coefficients in this region. The time delay is hardly influenced by the change in angle of attack.

Conclusions

Inhomogeneous flows occurring in several atmospheric phenomena may lead to dangerous situations for flight safety. As concerns the field of aerodynamics, only a few investigations have been undertaken to understand and to quantify the influence of inhomogeneous flows. Therefore, numerical simulations are performed concerning two cases of inhomogeneous flow for a NACA 0012 airfoil using an Euler code. With regard to an idealized shear wind, it can be seen that a velocity gradient in incoming flow has an important influence on the pressure distribution of the airfoil. For the presented cases, a positive gradient causes a positive additional lift and a negative moment around the 25% axis. In the transonic region, an incoming flow with velocity gradient influences considerably shock strength and shock position. The velocity regime, the velocity gradient, the position of the airfoil in the shear wind field, the angle of attack, and, in the unsteady case, the airfoil vertical velocity are studied as governing parameters concerning shear winds. As a realistic example, the flight through a microburst is analyzed, using a potential model for describing the incoming flowfield. The simulation gives rapid changes in lift and moment, mostly governed by the vertical velocity. These changes may be dangerous and can lead to loss of control during flight. Therefore, strong efforts have to be made to analyze this important field of aerodynamics further. Two major points for future work are investigations of three-dimensional flows around wings or aircraft configurations and the consideration of viscous effects using a Navier–Stokes code.

References

[1] Schänzer, G., "Influence of Windshear, Downdraft and Turbulence on Flight Safety," CP-470, AGARD, 1989, pp. 7-1–7-19.

[2] Jacobi, C., Siemer, A. H., and Roth, R., "Starke Windscherungen unter nicht extremen meteorologischen Bedingungen," *Sicherheit im Luftverkehr*, Deutsche Forschungsgemeinschaft, G. Schänzer, Wiley–VCH, Weinheim, Germany, 1997, pp. 111–123.

[3] Reiter, E. R., *Meteorologie der Strahlströme (Jet Streams)*, Springer-Verlag, Wien, Austria, 1961, pp. 1–3, 105–112, 206–212.

[4] Krauspe, P., "Beiträge zur Längsbewegung von Flugzeugen in Windscherungen," Ph.D. Thesis, Lehrstuhl für Flugmechanik, Technische Universität Braunschweig, Braunschweig, Germany, June 1983.

[5] Ruscheweyh, H., *Dynamische Windwirkung an Bauwerken*, Band 2: Praktische Anwendungen, Bauverlag GmbH, Wiesbaden, Germany, 1982, pp. 15–17.

[6] Zhu, S., and Etkin, B., "Model of the Wind Field in a Downburst," *Journal of Aircraft*, Vol. 22, No. 7, 1985, pp. 595–601.

[7] Lundgren, T. S., Yao, J., and Mansour, N. N., "Microburst Modelling and Scaling," *Journal of Fluid Mechanics*, Vol. 239, June 1992, pp. 461–488.

[8] Bobbitt, R. B., and Howard, R. M., "Escape Strategies for Turboprop Aircraft in Microburst Windshear," *Journal of Aircraft*, Vol. 29, No. 5, 1992, pp. 745–752.

[9] Grantham, W. J., Roetcisoender, G. G., and Parks, E. K., "DFW Microburst Model Based on AA-539 Data," *Journal of Aircraft*, Vol. 27, No. 11, 1990, pp. 917–922.

[10] Ghazi, M., and Al-Bahi, A., "Effect of Atmospheric Disturbances on Airplane Response," AIAA Paper 92-4340, 1992.

[11] McCarthy, J., Wilson, J., and Fujita, T. T., "The Joint Airport Weather Studies (JAWS) Project," *Bulletin of the American Meteorological Society*, Vol. 63, No. 1, 1982, pp. 15–22.

[12] Hjelmfelt, M. R., Orville, H. D., Roberts, R. D., Chen, J. P., and Kopp, F. J., "Observational and Numerical Study of a Microburst Line-Producing Storm," *Journal of the Atmospheric Sciences*, Vol. 46, No. 17, 1989, pp. 2731–2743.

[13] Pélegrin, M., "Aspekte der Flugsicherheit bei der Wechselwirkung zwischen Flugzeug und Atmosphäre," *Sicherheit im Luftverkehr*, Deutsche Forschungsgemeinschaft, G. Schänzer, Wiley-VCH, Weinheim, Germany, 1997, pp. 43–80.

[14] Schultz, T. A., "Multiple Vortex Ring Model of the DFW Microburst," *Journal of Aircraft*, Vol. 27, No. 2, 1990, pp. 163–168.

[15] White, R. J., "Effect of Wind Shear on Airspeed During Airplane Landing Approach," *Journal of Aircraft*, Vol. 29, No. 2, 1992, pp. 237–242.

[16] Ivan, M., "A Ring-Vortex Downburst Model for Flight Simulations," *Journal of Aircraft*, Vol. 23, No. 3, 1986, pp. 232–236.

[17] Vicroy, D. D., "Assessment of Microburst Models for Downdraft Estimation," *Journal of Aircraft*, Vol. 29, No. 6, 1992, pp. 1043–1048.

[18] Psiaki, M. L., and Stengel, R. F., "Optimal Flight Paths Through Microburst Wind Profiles," *Journal of Aircraft*, Vol. 23, No. 8, 1986, pp. 629–635.

[19] Ávila de Melo, D., and Hansman, R. J., "Analysis of Aircraft Performance During Lateral Maneuvering for Microburst Avoidance," *Journal of Aircraft*, Vol. 28, No. 12, 1991, pp. 837–842.

[20] Frost, W., Chang, H., McCarthy, J., and Elmore, K., "Aircraft Performance in a JAWS Microburst," *Journal of Aircraft*, Vol. 22, No. 7, 1985, pp. 561–567.

[21] Ruden, P., "Theorie des Tragflügelprofiles in der Nachbarschaft sprunghafter Gesamtdruckänderungen," *Jahrbuch der deutschen Luftfahrtforschung*, 1939, pp. I98–I113.

[22] Tsien, H., "Symmetrical Joukowsky Airfoils In Shear Flow," *Quaterly of Applied Mathematics*, Vol. 1, No. 2, 1943, pp. 130–148.

[23] Weissinger, J., "Linearisierte Profiltheorie bei ungleichförmiger Anströmung, Teil II: Schlanke Profile," *Acta Mechanica*, Vol. 13, Springer-Verlag, Wien, Austria, 1972, pp. 133–154.

[24] Ludwig, G. R., and Erickson, J. C., "Airfoils in Two-Dimensional Nonuniformly Sheared Slipstreams," *Journal of Aircraft*, Vol. 8, No. 11, 1971, pp. 874–880.

[25] Gupta, A. K., and Sharma, S. C., "Cambered Joukowsky Airfoil in a Nonuniform Weak Shear Flow," *Journal of Aircraft*, Vol. 11, No. 10, 1974, pp. 653–656.

[26] Küchemann, D., *The Aerodynamic Design of Aircraft*, Pergamon Press, Oxford, England, U.K., 1978, pp. 305–313.

[27] Brenneis, A., "Berechnung instationärer zwei- und dreidimensionaler Strömungen um Tragflügel mittels eines impliziten Relaxationsverfahrens zur Lösung der Eulergleichungen," Verein deutscher Ingenieure Fortschrittsberichte, Reihe 7: Strömungstechnik, Nr. 165, Verein Deutscher Ingenieure Verlag, Düsseldorf, Germany, 1989.

[28] Habibie, I. A., "Eulerlösungen für instationär längsbeschleunigte Strömungen um Tragflügelprofile," Ph.D. Thesis, Lehrstuhl für Fluidmechanik, Technische Universität München, München, Germany, July 1994.

[29] Fletcher, C. A. J., *Computational Techniques for Fluid Dynamics*, Vol. 2, Springer-Verlag, Berlin, 1988, pp. 48, 49.

[30] Rochholz, H., "Eulerlösungen für den Separationsvorgang von Träger/Orbiter-Systemen im Hyperschall," Ph.D. Thesis, Lehrstuhl für Fluidmechanik, Technische Universität München, München, Germany, Aug. 1994.

[31] Yee, H. C., "Upwind and Symmetric Shock-Capturing Schemes," NASA TM 89464, 1987.

[32] Weishäupl, C., "Tragflügelprofile in inhomogener Strömung," Ph.D. Thesis, Lehrstuhl für Fluidmechanik, Technische Universität München, München, Germany, Oct. 1998.

[33] Hirsch, C., *Numerical Computation of Internal and External Flows,* Vol. 2, Wiley, New York, 1995, pp. 138–149, 176–195.

[34] Kroll, N., "Berechnung von Strömungsfeldern um Propeller und Rotoren im Schwebeflug durch die Lösung der Euler-Gleichungen," DLR-FB 89-37, Ph.D. Thesis, Institut für Entwurfsaerodynamik, Deutsche Forschungsanstalt für Luft- und Raumfahrt, Braunschweig, Germany, June 1989.

[35] Thompson, J., Warsi, Z., and Mastin, C., *Numerical Grid Generation, Foundations and Applications*, North-Holland, Amsterdam, 1985, pp. 193–202.

[36] Sonar, T., "Grid Generation Using Elliptic Partial Differential Equations," DFVLR-FB 89-15, 1989.

[37] Eberle, A., "MBB-EUFLEX. A New Flux Extrapolation Scheme Solving the Euler Equations for Arbitrary 3–D Geometry and Speed," TR MBB-LKE122/S/PUB/140, München, 1984.

[38] Heller, G., "Aerodynamik von Deltaflügelkonfigurationen bei Schieben und Gieren," Ph.D. Thesis, Lehrstuhl für Fluidmechanik, Technische Universität München, München, Germany, May 1997.

[39] Fujita, T. T., "Tornadoes and Downbursts in the Context of Generalized Planetary Scales," *Journal of the Atmospheric Sciences*, Vol. 38, No. 8, 1981, pp. 1511–1534.